Two-phase dynamic MPM formulation for unsaturated soil ⋆

Francesca Ceccato[a], Alba Yerro[b], Veronica Girardi[a], Paolo Simonini[a]

[a] *University of Padua*
Department of Civil, Environmental and Architectural Engineering
Via Ognissanti 39, Padua, Italy
[b] *Virginia Polytechnic Institute and State University, Department of Civil and Environmental Engineering*
750 Drillfield Drive, 200 Patton Hall, Blacksburg, VA, US

Abstract

In this paper, a computational framework based on the Material Point Method is developed to study the coupled seepage-deformation process in unsaturated soils. Governing equations are derived from the balance equations of solid and liquid phases accounting for partial saturation effects, and the soil is discretized with a single set of material points which move according to the displacement of the solid phase. The implementation of different types of boundary conditions, such as transient hydraulic head, seepage face, and infiltration/evaporation, is discussed in detail. The method is applied to simulate levee collapse due to rapid drawdown and rainfall. The methodology proposed in this paper is a promising tool to advance the current practice, which customarily evaluates slope safety only by means of small deformation analyses based on FEM or LEM, while here a large deformation approach is presented.

Keywords: MPM, unsaturated soil, large deformations, dynamic coupled analysis, infiltration, seepage

1. Introduction

Many natural hazards involve large deformations of unsaturated soils, e.g. rainfall-induced landslides, embankment collapses due to wetting, seepage-induced instabilities of dams and levees, etc. The study of these phenomena requires to account for the complex hydromechanical interactions between solid skeleton and pore fluid and to model large deformations in order to predict the post-failure behaviour, which poses significant computational challenges. In common practice, the safety of these slopes is evaluated calculating a factor of safety (FS) with Finite Element Methods (FEMs) implementing hydromechanically coupled formulations or using Limit Equilibrium Methods (LEMs) [1, 2]. Standard Lagrangian FEMs can be used to derive the deformations of the slope under different boundary conditions, but the solution is limited to small displacements.

FS of a slope can be obtained with the shear strength reduction method in which the strength parameters are progressively reduced until the convergence to static equilibrium is impossible to

⋆The final version of the manuscript can be downloaded at https://doi.org/10.1016/j.compgeo.2020.103876. Cite as: Ceccato, F., Yerro, A., Girardi, V., Simonini, P. (2021) Two-phase dynamic MPM formulation for unsaturated soil. Computers and Geotechnics, 129, 103876.

reach [1]. With this approach, the shape of the failure surface results from the analysis. Differently, LEMs assume the shape of the sliding surface and compute FS as the ratio between the soil shear resistance and the mobilized shear stress along the surface. The pore pressure and effective stress distribution can be evaluated with preliminary FEM analyses. Since soil is assumed rigid-plastic, LEMs do not provide any information on the deformations.

The results of these analyses allow to evaluate FS at different time instants accounting for stress changes induced by various types of boundary conditions and the corresponding most likely failure mechanisms, but the evolution of the collapse cannot be assessed. The knowledge of failure evolution is important for risk management and planning of attenuation measures. Hence there is a need to develop solution schemes that are capable of simulating failure initiation as well as post-failure dynamics. To this end, a numerical method suitable for large deformation problems is necessary. Several methods have been proposed in the last decades to overcome the difficulties arising with FEM, e.g. ALE, CEL, PFEM, FEMLIP, SPH, MPM etc. A review of these methods applied to landslide mass movements can be found in Soga et al. [3]. Among them, the Material Point Method (MPM) has recently increased its popularity in the geotechnical community and it has been successfully applied in a number of problems involving multiphase interactions in soils [4, 5, 6, 7, 8, 9, 10, 11].

MPM was initially formulated for one-phase materials in solid mechanics by Sulsky et al. [12] and a number of numerical improvements have been developed since then. In MPM, the body is discretized by a cloud of material points (MPs), which move attached to the material and carry all the updated information such as velocities, strain, stresses, and state variables. Large deformations are simulated by MPs moving through a computational grid that covers the full problem domain. This grid is used to solve the system of equilibrium equations, but does not deform with the body like in Lagrangian FEM.

A number of mathematical formulations have been proposed in the literature for unsaturated soils based on different assumptions and using different primary unknown variables. Zienkiewicz et al. [13] present several formulations for saturated and unsaturated soils referring to FEM implementations and discuss their applicability for different kinds of problems in geomechanical engineering. These formulations can also be extended for MPM.

Recent developments of MPM for unsaturated soils include the work by Yerro et al. [4], which proposed a three-phase approach in which the governing equations are derived from the momentum balance and the mass balance equations of solid, liquid and gas phase assuming non-zero gas pressure. In this approach the primary unknowns are the absolute accelerations of the phases ($a_S - a_L - a_G$ formulation). The formulation is Lagrangian for the solid phase; MPs move with the kinematic of the solid skeleton, but carry the information of all phases (*single-point approach*). In contrast, Bandara et al. [7], Wang et al. [10] and Lei et al. [11] used a simplified approach, which neglects the momentum and the mass balance equations of the gas, thus reducing the computational cost. Bandara et al. [7] used a formulation derived from Biot's phenomenological approach in which the solid skeleton is represented using material coordinates and fluid motion is represented in terms of average relative velocity with respect to the solid skeleton (seepage velocity, w). Relative fluid acceleration and its convective terms are assumed negligible. Acceleration of solid skeleton and seepage velocity are the primary unknowns ($a_S - w$ formulation). In the formulation proposed in Wang et al. [10] the governing equations are derived from the dynamic equilibrium of the liquid phase and the mixture and the primary unknowns are the absolute accelerations of the solid and the liquid ($a_S - a_L$ formulation). The spatial gradient of liquid volumetric fraction is neglected in the liquid mass balance equation and this is acceptable when considering problems where the degree of saturation varies in a limited range and the slope

of the soil-water retention curve (SWRC) is small [14]. Lei et al. [11] extended this approach to include soil erosion. Governing equations for describing skeleton deformation, liquid flow, liquefaction of solid fine particles, and convection of liquidised fine particles are formulated for the explicit dynamic MPM framework, and discretized by the Generalized Interpolation Material Point (GIMP) method.

This paper presents a two-phase dynamic MPM formulation for non-erodible unsaturated soils based on the $a_S - a_L$ formulation. Governing equations are derived from the balance equations of solid and liquid phases and the soil is discretized with a single set of MPs which move according to the displacement of the solid phase, i.e. a *two-phase single-point* approach is used. Unlike previous works, here liquid acceleration and gradients of liquid volumetric fraction are accounted, which renders the formulation more suitable for dynamic problems where wave propagation is important [15, 16] and cases with large changes in suctions and degree of saturation [14]. The implementation in the MPM framework of foundamental boundary conditions, such as transient hydraulic head, seepage face, and infiltration/evaporation, is discussed in detail. These conditions are necessary to simulate typical geomechanical problems with unsaturated soils, but they have not been presented before. Indeed [4, 10, 11] simulated rainfall infiltration in a simplified way, considering full soil saturation at the boundary and did not present other types of hydraulic boundary conditions.

The paper is organized as follows. Section 2 presents the details of the governing equations, followed by Section 3 where the MPM formulation is derived. The implementation is validated in Section 4 by comparing MPM results with a commercial FEM code. Finally, its applicability to real cases is shown in Section 5 by considering two common causes of levee collapse: (i) rapid drawdown and (ii) seepage combined with heavy rainfall.

The proposed methodology allows to investigate failure and post-failure evolution of slopes in a unified numerical framework, thus offering a more comprehensive understanding of the phenomenon compared to the current practice based on LEM or FEM. The study is also relevant for authorities and practitioner involved in the field of geo-environmental risk assessment as the methodology can improve the design of efficient and cost-effective mitigation measures.

2. Governing equations

Unsaturated porous media are a mixture of three different phases: solid (S), liquid (L) and gas (G). The solid phase is made by solid grains that constitutes the solid skeleton of the media; meanwhile the liquid and the gas phases fill the voids. A comprehensive hydromecanically coupled formulation for unsaturated soils should consider the balance equations of each phase and the interaction between them. However, in many cases the presence of the gas phase can be accounted in a simplified way, thus reducing the computational cost.

In this paper, the following assumptions are adopted:

1. Gas pressure is neglected ($p_G = 0$)
2. Gas density is negligible compared to liquid and solid ones ($\rho_G \approx 0$)
3. Compressibility of solid grains is negligible compared to solid skeleton one ($\rho_S \approx 0$)
4. Isothermal conditions

The formulation is derived considering dynamic momentum balance of the liquid phase, dynamic momentum balance of the mixture, and mass balances and constitutive relationships of both phases involved (i.e. solid and liquid). All dynamic terms are taken into account; acceleration of the solid skeleton $\mathbf{a}_\mathrm{S}$ and acceleration of the pore liquid $\mathbf{a}_\mathrm{L}$ are the primary unknowns.

Unsaturated conditions are accounted considering that the liquid phase does not fill entirely the voids. The balance equations of gas phase are neglected, thus the presented formulation can be considered two-phase and is an extension of the one presented in Jassim et al. [17] and Wang et al. [10].

The momentum balance of the liquid phase per unit of liquid volume is given in Eq. 1,

$$\rho_{\mathrm{L}}\mathbf{a}_{\mathrm{L}} = \nabla p_{\mathrm{L}} - \mathbf{f}_{\mathrm{L}}^{\mathrm{d}} + \rho_{\mathrm{L}}\mathbf{g} \tag{1}$$

where ρ_{L} is the liquid density, $\mathbf{f}_{\mathrm{L}}^{\mathrm{d}}$ is the drag force which accounts for solid-fluid interaction, p_{L} is the liquid pressure and $\mathbf{g}$ is the gravity vector.

The flow is considered laminar and stationary in the slow velocity regime. Hence, the drag force is governed by Darcy's law (Eq. 2),

$$\mathbf{f}_{\mathrm{L}}^{\mathrm{d}} = \frac{n_{\mathrm{L}}\mu_{\mathrm{L}}}{\kappa_{\mathrm{L}}}\left(\mathbf{v}_{\mathrm{L}} - \mathbf{v}_{\mathrm{S}}\right) \tag{2}$$

where μ_{L} is the dynamic viscosity of the liquid, κ_{L} is the liquid intrinsic permeability, n_{L} is the liquid volumetric fraction and $\mathbf{v}_{\mathrm{L}}$, $\mathbf{v}_{\mathrm{S}}$ are the absolute liquid and solid velocities respectively.

The isotropic intrinsic permeability of the liquid κ_{L} can also be expressed in terms of Darcy permeability, or hydraulic conductivity, k_{L} (Eq. 3).

$$\kappa_{\mathrm{L}} = k_{\mathrm{L}}\frac{\mu_{\mathrm{L}}}{\rho_{\mathrm{L}}g} \tag{3}$$

The mixture dynamic momentum conservation can be written as Eq. 4,

$$n_{\mathrm{S}}\rho_{\mathrm{S}}\mathbf{a}_{\mathrm{S}} + n_{\mathrm{L}}\rho_{\mathrm{L}}\mathbf{a}_{\mathrm{L}} = \mathrm{div}(\sigma) + \rho_{\mathrm{m}}\mathbf{g} \tag{4}$$

where ρ_{S} is the solid grain density, n_{S} is the volumetric concentration ratio of solid, and $\rho_{\mathrm{m}} = n_{\mathrm{S}}\rho_{\mathrm{S}} + n_{\mathrm{L}}\rho_{\mathrm{L}}$ is the density of the mixture. Note that $n_{\mathrm{S}} = 1 - n$ and $n_{\mathrm{L}} = S_L n$, where n is the porosity of the solid skeleton and S_L is the degree of saturation. σ is the total stress tensor, which can be computed with the Bishop's effective stress equation for unsaturated soils and has the form of Eq. 5, where χ is an effective stress parameter, here assumed equal to S_L, and $\mathbf{m}$ is the unit vector, equal to $(1\ 1\ 1\ 0\ 0\ 0)^{\mathrm{T}}$ in 3D. In this paper, stresses and pressures are positive for tension, thus suction is equal to p_L.

$$\sigma = \sigma' + \chi p_L \mathbf{m} \tag{5}$$

The mass conservation of the solid phase is expressed as given in Eq. 6,

$$\frac{\partial(n_{\mathrm{S}}\rho_{\mathrm{S}})}{\partial t} + \mathrm{div}(n_{\mathrm{S}}\rho_{\mathrm{S}}\mathbf{v}_{\mathrm{S}}) = 0 \tag{6}$$

where $\mathbf{v}_{\mathrm{S}}$ is the velocity of the solid phase.

Similarly, the conservation of liquid mass can be written as Eq. 7,

$$\frac{\partial(n_{\mathrm{L}}\rho_{\mathrm{L}})}{\partial t} + \mathrm{div}(n_{\mathrm{L}}\rho_{\mathrm{L}}\mathbf{v}_{\mathrm{L}}) = 0 \tag{7}$$

where $\mathbf{v}_{\mathrm{L}}$ is the (true) velocity of the liquid phase

The material derivative with respect to the solid can be expressed as

$$\frac{\mathrm{D}^{\mathrm{S}}(\bullet)}{Dt} = \frac{\partial(\bullet)}{\partial t} + \mathbf{v}_{\mathrm{S}}\nabla(\bullet) \tag{8}$$

When considering incompressible solid grains and disregarding the spatial variations in density and porosity, the expressions for the conservation of mass of the solid and the liquid reduce to Eqs. 9 and 10 respectively.

$$\frac{\mathrm{D}^{\mathrm{S}} n_{\mathrm{S}}}{\mathrm{D}t} + n_{\mathrm{S}}\mathrm{div}(\mathbf{v}_{\mathrm{S}}) = 0 \tag{9}$$

$$\frac{\mathrm{D}^{\mathrm{S}}(\rho_{\mathrm{L}} n_{\mathrm{L}})}{\mathrm{D}t} = (\mathbf{v}_{\mathrm{S}} - \mathbf{v}_{\mathrm{L}})\nabla(n_{\mathrm{L}}\rho_{\mathrm{L}}) - n_{\mathrm{L}}\rho_{\mathrm{L}}\mathrm{div}(\mathbf{v}_{\mathrm{L}}) \tag{10}$$

Including Eq. 9 into Eq. 10, taking into account the definitions of liquid volumetric concentration ratios in terms of porosity and degree of saturation, $n_L = S_L n$, and rearranging terms give Eq. 11

$$n\frac{\mathrm{D}^{\mathrm{S}}(\rho_{\mathrm{L}} S_{\mathrm{L}})}{\mathrm{D}t} = \mathrm{div}\left[\rho_{\mathrm{L}} n S_{\mathrm{L}}(\mathbf{v}_{\mathrm{S}} - \mathbf{v}_{\mathrm{L}})\right] - \rho_{\mathrm{L}} S_{\mathrm{L}}\mathrm{div}(\mathbf{v}_{\mathrm{S}}) \tag{11}$$

Finally, the material derivative in Eq. 11 is solved assuming liquid pressure as state variable, which yields to Eq. 12.

$$n\left(S_{\mathrm{L}}\frac{\partial \rho_{\mathrm{L}}}{\partial p_{\mathrm{L}}} + \rho_{\mathrm{L}}\frac{\partial S_{\mathrm{L}}}{\partial p_{\mathrm{L}}}\right)\frac{\mathrm{D}^{\mathrm{S}} p_{\mathrm{L}}}{\mathrm{D}t} = \mathrm{div}\left[\rho_{\mathrm{L}} n S_{\mathrm{L}}(\mathbf{v}_{\mathrm{S}} - \mathbf{v}_{\mathrm{L}})\right] - \rho_{\mathrm{L}} S_{\mathrm{L}}\mathrm{div}(\mathbf{v}_{\mathrm{S}}) \tag{12}$$

The derivative of liquid density with respect of pressure is given by the state equation of liquid; while the derivative of the degree of saturation is given by the soil-water retention curve (SWRC).

When neglecting the spatial variability of porosity and degree of saturation, i.e $\nabla(\rho_L n S_L) \approx 0$, Eq. 12 can be simplified in Eq. 13

$$n\left(S_{\mathrm{L}}\frac{\partial \rho_{\mathrm{L}}}{\partial p_{\mathrm{L}}} + \rho_{\mathrm{L}}\frac{\partial S_{\mathrm{L}}}{\partial p_{\mathrm{L}}}\right)\frac{\mathrm{D}^{\mathrm{S}} p_{\mathrm{L}}}{\mathrm{D}t} = \rho_{\mathrm{L}} n S_{\mathrm{L}}\mathrm{div}(\mathbf{v}_{\mathrm{S}} - \mathbf{v}_{\mathrm{L}}) - \rho_{\mathrm{L}} S_{\mathrm{L}}\mathrm{div}(\mathbf{v}_{\mathrm{S}}) \tag{13}$$

This simplified form has been adopted by Wang et al. [10]. Yerro et al. [18], Ceccato et al. [14] showed that the use of Eq. 13 gives reasonably good results for applications where the degree of saturation varies in a limited range and the derivative of the SWRC is small. In this paper, the more general Eq. 12 is used to update liquid pressure.

Hydraulic and mechanical constitutive equations are used to close the system of governing equations as explained in the following sections.

2.1. Mechanical constitutive equation

In unsaturated soils, two stress variables can be used to capture the soil behaviour, e.g. net stress $\sigma_{\mathrm{net}} = \sigma - p_G$ and suction $s = p_L - p_G$. The incremental stress-strain equation becomes Eq. 14,

$$\frac{\mathrm{D}^{\mathrm{S}}\sigma_{\mathrm{net}}}{\mathrm{D}t} = \mathbf{D}^{\mathrm{ep}}\frac{\mathrm{D}^{\mathrm{S}}\varepsilon}{Dt} + \mathbf{h}'\frac{\mathrm{D}^{\mathrm{S}} s}{Dt} \tag{14}$$

where $\mathbf{D}^{\mathrm{ep}}$ is the tangent stiffness matrix, $\mathbf{h}'$ is a constitutive vector. Both are defined by the constitutive model.

A great number of constitutive models for unsaturated soils have been presented in the literature [19, 20, 21, 22, 23, 24], but in this paper a basic elastoplatic model with Mohr-Coulomb failure criterion is used. More advanced constitutive models for unsaturated soils can be easily employed in order to capture more accurately the soil behaviour.

2.2. Hydraulic constitutive equation

The relationship between pore liquid pressure and degree of saturation or liquid content is essential to model the behaviour of unsaturated soil. This is given by the SWRC which can assume different analytical expressions. In the following, two alternative relationships are used: (i) a linear relation (Eq. 15) where a_v is a constant parameter, S_{min} is the residual degree of saturation and S_{max} is the maximum degree of saturation, and (ii) the Van Genuchten relationship (Eq. 16) where p_{ref}, λ, are fitting parameters.

$$S_L = S_{min} + (S_{max} - S_{min}){p_L}^{a_v} \tag{15}$$

$$S_L = S_{min} + (S_{max} - S_{min})\left[1 + \left(\frac{p_L}{p_{ref}}\right)^{\frac{1}{1-\lambda}}\right]^{-\lambda} \tag{16}$$

Partial saturation modifies the soil hydraulic conductivity; in general partially saturated soils are less permeable than fully saturated soils. The ratio between actual hydraulic conductivity and saturated hydraulic conductivity k/k_{sat} is a function of the degree of saturation as given by the hydraulic conductivity curve (HCC). A number of relationships has been proposed in the literature, the functions proposed by Hillel [25] (Eq. 17) and Mualem [26] (Eq. 18) are implemented in the applied software, in which r and λ are fitting parameters.

$$\frac{k}{k_{sat}} = S_L^r \tag{17}$$

$$\frac{k}{k_{sat}} = \sqrt{S_L}\left[1 - (1 - S_L^{\frac{1}{\lambda}})^{\lambda}\right]^2 \tag{18}$$

3. MPM formulation

3.1. Discretized equations

The discretized equations (Eqs. 19, 20) are obtained by deriving the weak form of the momentum balance equations (Eqs. 1 and 4), using the Galerkin procedure, and approximating the acceleration and velocity fields by means of finite element shape functions $\mathbf{N}$.

$$\widetilde{\mathbf{M}}_{\mathrm{L}}\mathbf{a}_{\mathrm{L}} = \mathbf{f}_{\mathrm{L}}^{\mathrm{ext}} - \mathbf{f}_{\mathrm{L}}^{\mathrm{int}} - \mathbf{Q}_{\mathrm{L}}(\mathbf{v}_{\mathrm{L}} - \mathbf{v}_{\mathrm{S}}) \tag{19}$$

$$\mathbf{M}_S\,\mathbf{a}_{\mathrm{S}} + \mathbf{M}_{\mathrm{L}}\mathbf{a}_{\mathrm{L}} = \mathbf{f}^{\,\mathrm{ext}} - \mathbf{f}^{\,\mathrm{int}} \tag{20}$$

$\mathbf{a}_{\mathrm{L}}$, $\mathbf{a}_{\mathrm{S}}$, $\mathbf{v}_{\mathrm{L}}$, and $\mathbf{v}_{\mathrm{S}}$ are the nodal acceleration and velocity vectors; $\mathbf{M}_{\mathrm{S}}$, $\mathbf{M}_{\mathrm{L}}$, and $\widetilde{\mathbf{M}}_{\mathrm{L}}$ are solid and liquid lumped mass matrices (Eq. 21-23); $\mathbf{f}_{\mathrm{L}}^{\mathrm{ext}}$, $\mathbf{f}_{\mathrm{L}}^{\mathrm{int}}$, $\mathbf{f}^{\,\mathrm{ext}}$, $\mathbf{f}^{\,\mathrm{int}}$ are internal and external nodal force vectors of the liquid phase and the mixture (Eqs. 24-27), and $\mathbf{Q}_{\mathrm{L}}$ is the drag force matrix (Eq. 28).

$$\widetilde{\mathbf{M}}_{\mathrm{L}} \approx \sum_{\mathrm{MP}=1}^{n_{\mathrm{MP}}} \widetilde{m}_{\mathrm{L}}^{\mathrm{MP}} \mathbf{N} \tag{21}$$

$$\mathbf{M}_{\mathrm{L}} \approx \sum_{\mathrm{MP}=1}^{n_{\mathrm{MP}}} m_{\mathrm{L}}^{\mathrm{MP}} \mathbf{N} \tag{22}$$

$$\mathbf{M}_{\mathrm{S}} \approx \sum_{\mathrm{MP}=1}^{n_{\mathrm{MP}}} m_{\mathrm{S}}^{\mathrm{MP}} \mathbf{N} \tag{23}$$

$$\mathbf{f}_{\mathrm{L}}^{\mathrm{ext}} \approx \int_{\partial\Omega_p} \mathbf{N}^{\mathrm{T}} \widehat{\mathbf{p}}_{\mathrm{L}} \mathrm{d}\partial\Omega_{\mathrm{p}} + \sum_{\mathrm{MP}=1}^{n_{\mathrm{NP}}} m_{\mathrm{L}}^{\mathrm{MP}} \mathbf{N}^{\mathrm{T}} \mathbf{g} \tag{24}$$

$$\mathbf{f}^{\mathrm{ext}} \approx \int_{\partial\Omega_\tau} \mathbf{N}^{\mathrm{T}} \tau \mathrm{d}\partial\Omega_\tau + \sum_{\mathrm{MP}=1}^{n_{\mathrm{MP}}} m_{\mathrm{m}}^{\mathrm{MP}} \mathbf{N}^{\mathrm{T}} \mathbf{g} \tag{25}$$

$$\mathbf{f}_{\mathrm{L}}^{\mathrm{int}} \approx \sum_{\mathrm{MP}=1}^{n_{\mathrm{MP}}} \mathbf{B}^{\mathrm{T}} p_{\mathrm{L}}^{\mathrm{MP}} \mathbf{m} V_{\mathrm{MP}} \tag{26}$$

$$\mathbf{f}^{\mathrm{int}} \approx \sum_{\mathrm{MP}=1}^{n_{\mathrm{MP}}} \mathbf{B}^{\mathrm{T}} \sigma_{\mathrm{MP}} V_{\mathrm{MP}} \tag{27}$$

$$\mathbf{Q}_{\mathrm{L}} \approx \sum_{\mathrm{MP}=1}^{n_{\mathrm{MP}}} \mathbf{N}^{\mathrm{T}} \frac{n_{\mathrm{L}}^{\mathrm{MP}} \rho_{\mathrm{L}} g}{k_{\mathrm{L}}^{\mathrm{MP}}} \mathbf{N} V_{\mathrm{MP}} \tag{28}$$

Where τ is the prescribed traction vector in the boundary $\partial\Omega_\tau$, $\widehat{\mathbf{p}}_{\mathrm{L}}$ is the prescribed liquid pressure in the boundary $\partial\Omega_p$, $\mathbf{N}$ is the matrix of nodal shape functions and $\mathbf{B}$ is the matrix of the gradients of the nodal shape functions evaluated at local MP positions. The treatment of boundary conditions for unsaturated soils is described in details in Sec. 3.3.

The phase mass of the MP is calculated as Eqs. 29-32, where V_{MP} is the volume of the MP.

$$\widetilde{m}_{\mathrm{L}}^{\mathrm{MP}} = \rho_{\mathrm{L}} V_{\mathrm{MP}} \tag{29}$$

$$m_{\mathrm{L}}^{\mathrm{MP}} = n_{\mathrm{L}}^{\mathrm{MP}} \rho_{\mathrm{L}} V_{\mathrm{MP}} \tag{30}$$

$$m_{\mathrm{S}}^{\mathrm{MP}} = n_{\mathrm{S}}^{\mathrm{MP}} \rho_{\mathrm{S}} V_{\mathrm{MP}} \tag{31}$$

$$m_{\mathrm{m}}^{\mathrm{MP}} = \rho_{\mathrm{m}} V_{\mathrm{MP}} \tag{32}$$

Eqs. 19 and 20 are integrated in time using the Euler-Cromer explicit method. This time integration scheme is conditionally stable and the critical time step size is computed as indicated in Mieremet et al. [27] and later extended in Mieremet [28].

The momentum balances (Eqs. 19 and 20) are discretised and solved at the nodes of the mesh as in Jassim et al. [17]. Mass balances (Eqs. 9 and 12) and constitutive equations (Eqs. 14) are posed locally at the MPs to update secondary variables.

3.2. Numerical algorithm

The formulation presented in previous section is implemented in the open source code Anura3D (www.anura3d.eu). The numerical algorithm is based on the modified lagrangian algorithm originally proposed by Sulsky et al. [29] for one-phase material, and successfully extended to multiphase materials (see e.g. [17, 4]). The MPM solution scheme for each time step can be summarised as follows.

1. Liquid momentum balance equation (Eq. 19) is assembled and solved for the liquid nodal acceleration $\mathbf{a}_{\mathrm{L}}$.
2. Mixture momentum balance equation (Eq. 20) is assembled and solved to obtain the nodal acceleration of the solid $\mathbf{a}_{\mathrm{S}}$.
3. Velocities and momentum of the MPs are updated from nodal accelerations of each phase.
4. Nodal velocities are calculated from nodal momentum and used to compute the strain increment at the MP location and the terms on the right-end-side of Eq. 12.
5. Mass balance equation (Eq. 12) and soil stress-strain equation (Eq. 14) give the increment of pore pressure and effective stress respectively.
6. State variables at MPs are updated. Degree of saturation and hydraulic conductivity are updated according to SWRC and HCC respectively.
7. Displacement and position of each MP are updated according to the updated velocity of the solid phase.
8. Nodal values are discarded, the MPs carry all the updated information, and the computational grid is initialised for the next time step.

Steps 1 and 2 are commonly referred to as *Lagrangian phase*, while steps 3 to 8 are called *convective* or *Eulerian phase* of the method to emphasize the fact that MPM combines the advantages of Lagrangian and Eulerian approaches.

3.3. Treatment of boundary conditions

The proposed formulation requires the definition of the following boundary conditions (BC):

1. prescribed liquid displacement or velocity on $\partial\Omega_{v_{\mathrm{L}}}$ and prescribed pressure on $\partial\Omega_{\mathrm{p}}$, where $\partial\Omega = \partial\Omega_{v_{\mathrm{L}}} \cup \partial\Omega_{\mathrm{p}}$ and $\partial\Omega_{v_{\mathrm{L}}} \cap \partial\Omega_{\mathrm{p}} = 0$
2. prescribed solid displacement or velocity on $\partial\Omega_{\mathrm{u}}$ and prescribed traction on $\partial\Omega_{\tau}$, where $\partial\Omega = \partial\Omega_{v_{\mathrm{S}}} \cup \partial\Omega_{\tau}$ and $\partial\Omega_{v_{\mathrm{S}}} \cap \partial\Omega_{\tau} = 0$.

Essential boundary conditions on $\partial\Omega_{v_{\mathrm{L}}}$ and $\partial\Omega_{v_{\mathrm{S}}}$ are imposed on the nodes of the computational grid. Natural boundary conditions on $\partial\Omega_{\mathrm{p}}$ and $\partial\Omega_{\tau}$ are included in the weak form of the momentum balance equations.

In typical problems with partially saturated soil in geomechanics, prescribed liquid velocity can be applied on infiltration boundaries as described in Sec. 3.3.2, and prescribed pressures can be applied either by defining a pressure load $\widehat{p_L}$ or by assigning a total hydraulic head $\widehat{H}$ as explained in Sec. 3.3.1. Assuming the validity of Bernoulli's equation and neglecting the kinematic head, the total hydraulic head can be written as

$$\widehat{H} = h_g - \frac{\widehat{p_L}}{\rho_L g} \tag{33}$$

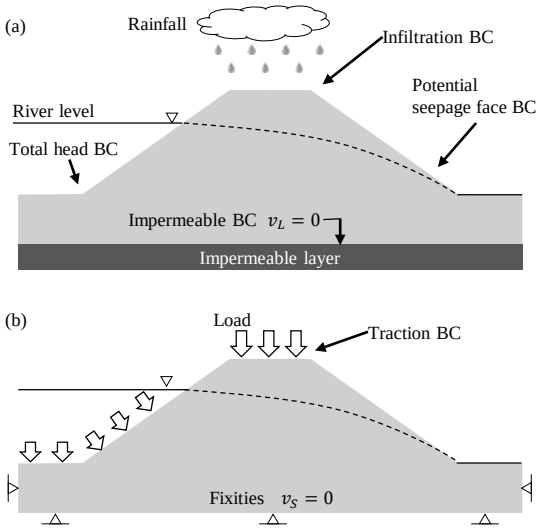

Figure 1: Typical boundary conditions for liquid phase (a) and mixture (b).

where h_g stands for the potential head or geometric head and $\widehat{p_L}/(\rho_L g)$ is the pressure head. The minus sign in Eq. 33 is introduced because pressure is assumed negative for compression.

Sometimes, the boundary condition is part of the problem solution, i.e. it is not known a priori if the boundary belongs to $\partial\Omega_{v_L}$ or $\partial\Omega_p$. This is typical of free surface flows across porous media along the so-called *potential seepage face* [30, 31]. Moreover, the size of this boundary condition can evolve along time. This boundary condition can be applied as presented in Sec. 3.3.3. Figure 1 represents schematically how these BCs simulate different hydraulic loading acting on a levee.

In classical FEM, the application of prescribed boundary conditions is simple as these can be specified directly on the boundary nodes, which coincide with the boundary of the continuum body and are well defined throughout the computation. However, the computational mesh in MPM does not necessarily align with the boundary of the material making the application of the prescribed boundary conditions more challenging. In the numerical framework proposed here, zero-traction and zero-pressure boundary conditions are automatically enforced to be satisfied by the solution of equations of motion, but difficulties arise when dealing with non-zero boundary conditions. The nodes belonging to the boundary are determined with a procedure similar to the surface boundary algorithm presented in Bandara and Soga [5], here extended for unstructured mesh. For each time step, firstly the active elements (i.e. elements containing MPs) adjacent to an empty element (i.e. element without MPs) are detected (*boundary elements*); then the nodes belonging to the element side adjacent to an empty element (*boundary side*) are marked as *boundary nodes*. The MPs next to the boundary side are identified as *boundary material points* as shown in Fig. 2. Finally, if the boundary node lies inside the area where a specified condition has to be applied, e.g. in the infiltration zone or on the potential seepage face, the corresponding boundary condition is applied.

Another difficulty with moving boundaries appears when prescribed velocity or traction (pressure) do not have a constant direction, but it is normal to the boundary. This means that

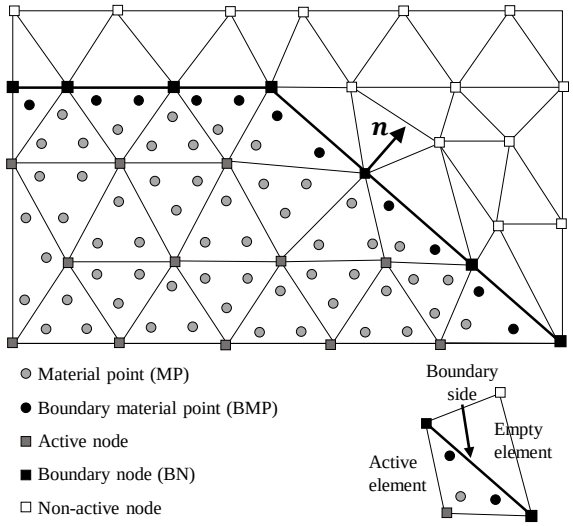

Figure 2: Definition of boundary nodes and boundary material points

if the shape of the contour changes, the direction of the applied condition has to be updated during the calculation. The normal direction at the node is determined by means of the gradient of mass as Eq. 34

$$\mathbf{n} \approx \frac{\sum_{\mathrm{MP}=1}^{n_{\mathrm{MP}}} m_m^{\mathrm{MP}} \mathbf{B}}{\| \sum_{\mathrm{MP}=1}^{n_{\mathrm{MP}}} m_m^{\mathrm{MP}} \mathbf{B} \|} \tag{34}$$

3.3.1. Hydraulic head BC

Examples in which hydraulic head BC can be used are the seasonal fluctuations of groundwater tables [32], impoundement or drawdown of a water reservoir [33], the sudden increase of river levels due to an extreme flood event, the rupture of buried water pipes altering the surrounding water table distribution in a urban environment, or the effect of introducing a drainage system to stabilize a slope.

The hydraulic head BC is converted to an imposed pressure condition $\widehat{p_L}$, using Eq. (33) solved for the liquid pressure. This means that a hydrostatic approximation is adopted, neglecting local turbulence induced by the river flow or by the potential collapse of the internal bank. The element's nodes affected by this condition are detected with the algorithm introduced in the previous section (Fig. 2).

A series of hydraulic head values in time, like the ones provided by water gauges readings, is assigned with an input file, and at each time step the current hydraulic head H_{curr} is computed by linear interpolation. The resulting nodal vector is part of the vector of external forces in the liquid momentum equation ($\mathbf{f}_{\mathrm{L}}^{\mathrm{ext}}$ in Eq. 19) and in the mixture momentum equation ($\mathbf{f}^{\mathrm{ext}}$ in Eq. 20) to account also for water weight.

Concerning the boundary nodes included in the hydraulic head BC but lying above H_{curr}, two

approaches are proposed: (i) constant pressure and (ii) linear pressure distribution (in suction), following the same hydrostatic gradient given by γ_W. In the case of a homogeneous slope in stationary flow regimes, it is common to introduce the unsaturated condition above the water table [34, 35], which reflects in the pore pressure distribution. Close to the phreatic surface, a linear increase of suction can be explained by the capillary rise controlled by the SWRC. The upper portion, closer to the interface with the atmosphere, is governed by climate conditions and suction depends on the water mass balance at the soil surface [35, 36]. The constant approximation reproduces this last effect, while the linear approximation simulates better the capillary effect. The drawback of the later approach is the overestimation of suction at higher locations. In the literature, the BC above the river level has been reproduced in different ways. In some cases, an infiltration/evaporation BC is applied [35, 36] or a zero nodal flux is imposed [37], in other cases the condition has been approximated with the use of a potential seepage face [30, 38].

3.3.2. Infiltration BC

This boundary condition is necessary to simulate rainfall or evaporation boundary condition. It consists in applying a prescribed specific discharge $q = \widehat{\mathbf{w}} \cdot \mathbf{n}$ along the boundary, where $\mathbf{n}$ is the outward normal unit vector (Eq. 34) and the seepage velocity $\widehat{\mathbf{w}}$ is defined as Eq. 35

$$\widehat{\mathbf{w}} = n_L(\mathbf{v}_L - \mathbf{v}_S) \tag{35}$$

The application of this boundary condition is based on a predictor-corrector scheme: liquid and solid velocity are first predicted assuming zero-pressure boundary conditions at the infiltration boundary and then (eventually) corrected to ensure the prescribed infiltration rate. The procedure can be summarized in the following steps, also shown in Fig. 3:

1. $\mathbf{a}_{\mathrm{L}}^t$ and $\mathbf{a}_{\mathrm{S}}^t$ are computed by solving Eqs. 19 and 20 assuming $\widehat{p_L} = 0$ at the infiltration boundary
2. Nodal velocities are predicted as $\tilde{\mathbf{v}}_L^{t+\Delta t} = \mathbf{v}_L^t + \mathbf{a}_{\mathrm{L}}\Delta t$ and $\tilde{\mathbf{v}}_S^{t+\Delta t} = \mathbf{v}_S^t + \mathbf{a}_{\mathrm{S}}\Delta t$
3. Infiltration condition is checked. If the net infiltration discharge q_{net} (Eq. 36) is positive, ponding conditions occur and if fluid accumulation above the boundary is not allowed (it must remain at zero pressure) no correction is necessary. If the net infiltration discharge is negative, or liquid ponding is allowed above the surface, then liquid velocity must be corrected to ensure the correct infiltration rate.

$$q_{net} = (n_L(\tilde{\mathbf{v}}_L^{t+\Delta t} - \tilde{\mathbf{v}}_S^{t+\Delta t}) - \widehat{\mathbf{w}}) \cdot \mathbf{n} \tag{36}$$

4. If necessary, the liquid nodal velocity is corrected by Eq. 37

$$\mathbf{v}_L^{t+\Delta t} = \tilde{\mathbf{v}}_L^{t+\Delta t} + \Delta\mathbf{v}_L \tag{37}$$

where $\Delta\mathbf{v}_L$ is derived by imposing $q_{net} = 0$ (Eq. 38) and it is given by Eq. 39.

$$(n_L(\tilde{\mathbf{v}}_L^{t+\Delta t} + \Delta\mathbf{v}_L - \tilde{\mathbf{v}}_S^{t+\Delta t}) - \widehat{\mathbf{w}}) \cdot \mathbf{n} = 0 \tag{38}$$

$$\Delta\mathbf{v}_L = ((n_L(\tilde{\mathbf{v}}_L^{t+\Delta t} - \tilde{\mathbf{v}}_S^{t+\Delta t}) - \widehat{\mathbf{w}}) \cdot \mathbf{n})\mathbf{n} \tag{39}$$

5. The corrected liquid acceleration is computed as $\mathbf{a}_{\mathrm{L}}^t = (\mathbf{v}_{\mathrm{L}}^{t+\Delta t} - \mathbf{v}_{\mathrm{L}}^t)/\Delta t$
6. The MPM solution scheme can proceed with the convective phase as explained in steps 3-8 of Sec. 3.2.

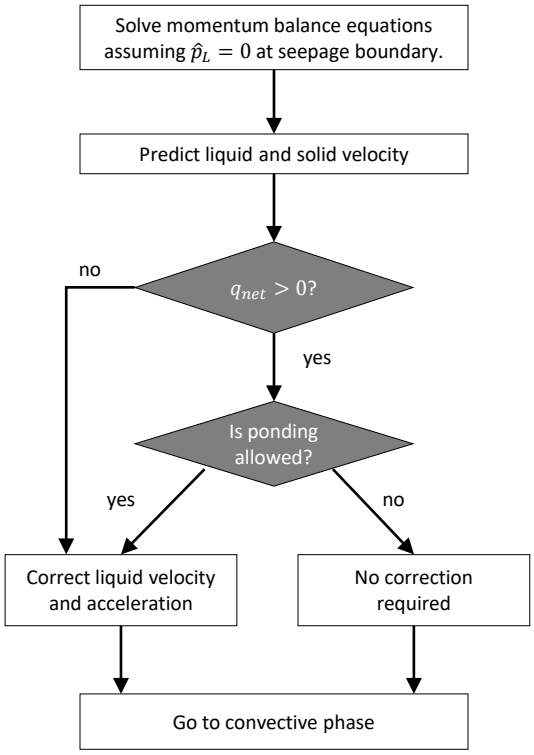

Figure 3: Flow chart of the infiltration boundary condition

Note that this boundary condition is applied at nodal level, thus nodal liquid volumetric fraction is necessary. This can be computed by mapping $n_L = nS_L$ from the MPs to the nodes of the mesh.

3.3.3. Potential seepage face BC

A *potential seepage face* can be defined as an interface between soil and atmosphere where the fluid is free to exit at zero pressure when the soil is saturated, but it cannot enter when the soil is partially saturated. An example of potential seepage face is the downstream surface of a river embankment (Fig. 1a), or it can also arise in after a rapid drawdown of the river level. This boundary condition is necessary where it is unknown if the boundary is an essential or a natural boundary condition.

The implementation can be considered as a special case of the infiltration boundary condition described in Sec. 3.3.2, where $\widehat{\mathbf{w}} = 0$. Liquid and solid nodal velocities are predicted assuming zero-pressure at the potential seepage face (natural boundary condition). If $(n_L(\tilde{\mathbf{v}}_L^{t+\Delta t} - \tilde{\mathbf{v}}_S^{t+\Delta t})) \cdot \mathbf{n} > 0$ it means that fluid is flowing out of the soil at zero pressure and no correction is required. If $(n_L(\tilde{\mathbf{v}}_L^{t+\Delta t} - \tilde{\mathbf{v}}_S^{t+\Delta t})) \cdot \mathbf{n} < 0$, then fluid is flowing into the soil at zero pressure, thus liquid velocity must be corrected with Eqs. 37 and 39 in which $\widehat{\mathbf{w}} = 0$ (switch to essential boundary condition).

4. Validation

Validating the presented formulation is not straightforward because no analytical solution is available for coupled soil deformation-fluid flow in unsaturated conditions. For this reason, the fluid-flow problem is validated in this section considering two simple benchmarks: (i) a 1D column infiltration (Sec. 4.1) and (ii) a 2D seepage flow (Sec. 4.2), by comparing the results obtained by MPM and the well-established FEM software SEEP/W by Geostudio. In FEM seepage analyses the deformation of the solid skeleton is neglected, analogously solid velocity is assumed to be zero in MPM.

4.1. 1D infiltration

A 1m-high soil column is considered with the material parameters listed in Tab. 1. For simplicity, the intrinsic permeability is assumed constant and equal to $\kappa_L = 1 \cdot 10^{-11} m^2/s$, corresponding to an hydraulic conductivity of $k = 1.0 \cdot 10^{-4}$m/s. Van Genuchten SWRC is accounted (Eq. 16), with parameters $p_{ref} = 3kPa$, $\lambda = 0.7$, $S_{min} = 0.125$, $S_{max} = 1$.

Solid density $[kg/m^3]$	ρ_S	2700
Liquid density $[kg/m^3]$	ρ_L	1000
Porosity [-]	n	0.4
Liquid bulk modulus $[kPa]$	K_L	80000
Liquid dynamic viscosity $[1/kPa]$	μ_L	$1 \cdot 10^{-6}$

Table 1: Material parameters for 1D infiltration example and 2D seepage flow.

The column is discretized with 20 rows of 2 square triangular elements filled with 3 MPs each (Fig. 4a). The bottom and lateral boundaries are impervious, while a vertical infiltration rate $\widehat{w}_y = 1.0 \cdot 10^{-4}$ m/s is applied at the top boundary. An initial suction of 2kPa is assigned at $t = 0$s along the column, which corresponds to an initial degree of saturation $S_{L0} = 0.87$.

The liquid infiltrates from the top and flows down though the column accumulating at the impervious bottom. Here suction starts decreasing and the soil saturates increasing S_L to 1. Fig. 4 plots the evolution of pore pressure and degree of saturation distribution along the column at different time instants. MPM results are in very good agreement with FEM. As expected, it can be noted that at long time ($t = 600s$) soil is saturated at the top boundary, i.e. $p_L = 0$, thus the infiltration BC switches from essential, i.e. applied infiltration velocity, to natural, i.e. zero-pressure, and the pore pressure does not increase further.

4.2. 2D seepage flow

The hydraulic head BC and the seepage BC are applied in a simple case of a river levee affected by seepage flow from the river side. A 1m-high river embankment is considered, with slopes 2/3 on the river side and 1/2 on the land side, as reported in Fig 5. The material parameters are summarized in Tab. 1. A linear SWRC (Eq. 15), with slope coefficient $a_v = 4.0 \cdot 10^{-4}$ 1/kPa is accounted, while the intrinsic permeability is constant and equals to $\kappa_L = 4 \cdot 10^{-11} m^2/s$, corresponding to an hydraulic conductivity of $k = 3.92 \cdot 10^{-4}$ m/s.

The initial phreatic level is at 0.0m, corresponding to the ground level at both levee's sides, visible in Fig.6a. Above the initial water table, the pore pressure is linearly approximated. The seepage face and the hydraulic head BCs are applied, respectively on the land and on the river side. The river level increases linearly during 180s, till its maximum value of 0.6m. Then, it

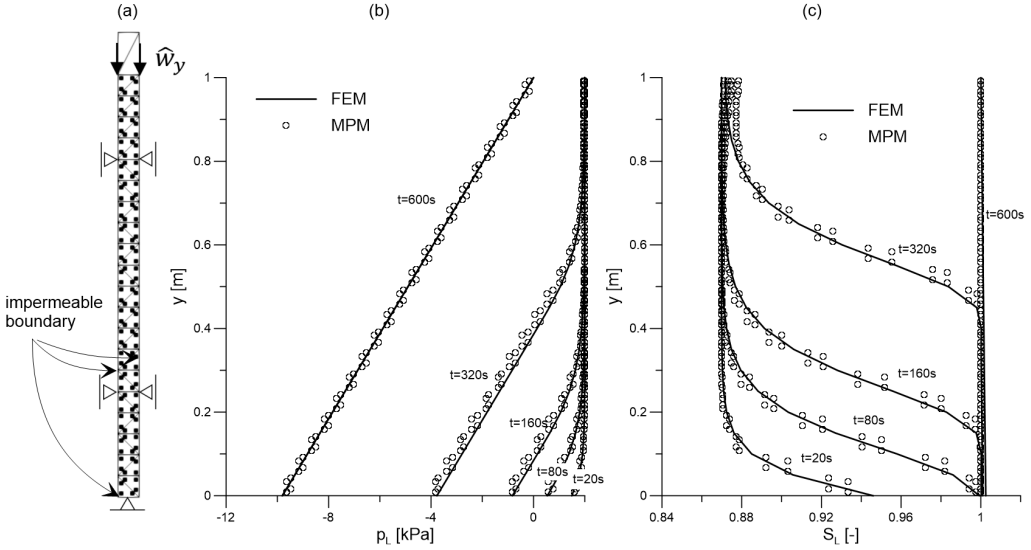

Figure 4: Geometry of the problem (a). Evolution of liquid pressure (b) and degree of saturation (c) along the column. Comparison between MPM and FEM.

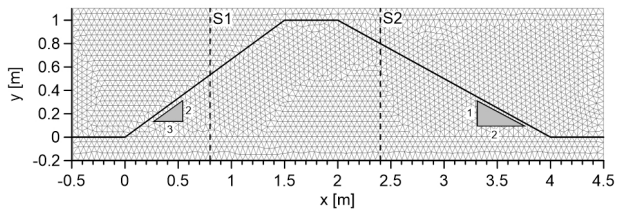

Figure 5: Geometry and mesh of the MPM model. Positions of sections S1 and S2.

remains constant until the end of the simulated time, equal to 200s. The mesh is unstructured, made of 3-nodes triangular elements of average size 0.05m. The FEM model mesh counts 2934 elements while, due to a wider covered domain, the MPM model counts 5660 elements; a number of 3 MPs is assigned to the elements belonging to the earth embankment.

Fig. 6 compares FEM and MPM results in terms of pore pressure distribution in the levee body at four increasing time instants (0s, 60s, 120s, and 200s). Furthermore, the phreatic line is highlighted with blue dots in MPM (corresponding to MPs with a pressure between -0.2 and 0.2kPa) and dashed blue lines in FEM, visualizing the progression of the saturated front in both models, according to the water level rise.

The progression along time is also shown in Fig. 7, where the pore water pressure distribution along two vertical sections (S1 and S2) is plotted at three different instants: 30s, 90s, and 180s. The fitting of the MPM values with FEM shows an overall good agreement, both in terms of entity and slope of the plotted curves. In the transient phase of the seepage flow, we observe a minor discrepancy between the trends, more evident along section S2, yet never greater than 1kPa.

Given that, these small gaps may be attributed to underpin diversities in the formulations. Indeed, MPM solves the dynamic momentum balance of the liquid, considering the liquid acceleration as primary unknown. The pressure increment is a secondary variable updated solving the mass balance equation. On the contrary, the FEM approach solves directly for the nodal pressure (or hydraulic head), without considering the liquid acceleration terms as in the MPM. In addition, solid skeleton and water compressibility may be the source of some minor differences. Nonetheless, the seepage flow is in agreement between the two numerical techniques, both in its spatial and temporal connotations.

5. Application examples

In this section, the formulation presented in Sec. 3 is applied to study the stability of a levee. Failure of dams and levees can be caused by several mechanisms, e.g. macro-instability, overtopping, erosion (internal and external) [39, 40, 41]. Here we focus on the macro-instabilities due to changes in the pore pressure regime induced by two typical phenomena schematically represented in Fig. 8a: (i) a rapid drawdown of the water level on the river side (Sec. 5.1) and (ii) infiltration due to heavy rainfall on the land side (Sec. 5.2). MPM results are compared with the ones obtained by FEM seepage analysis coupled with LEM analysis to evaluate FS.

The considered levee is 3m-high with a slope inclination of 2/3. A low-permeability layer is assumed to lie at a depth of 0.5m, here simulated with an impermeable boundary. The levee is assumed to be symmetric, thus the same geometry and discretization is used in both the drawdown and the rainfall case. The geometry and mesh discretization is shown in Fig. 8b. For computational efficiency, only half of the levee section is discretized. The model counts a total of 1669 linear triangular elements and 897 nodes. The average element size on the slope is 0.2m. 3 MPs are placed inside each initially active element. For the seepage analysis, a mesh of the same average size and type is used in the FEM model, for a total of 1158 elements. LEM analysis applies Bishop method.

A linear SWRC, with slope coefficient $a_v = 4.0 \cdot 10^{-4}$ 1/kPa is used, and the hydraulic conductivity is assumed constant. This permeability is higher than commonly found in these structures, and allows to reduce the simulated time and computational cost. An elastic-perfectly plastic Mohr Coulomb constitutive model is adopted to model the soil behavior, with the material

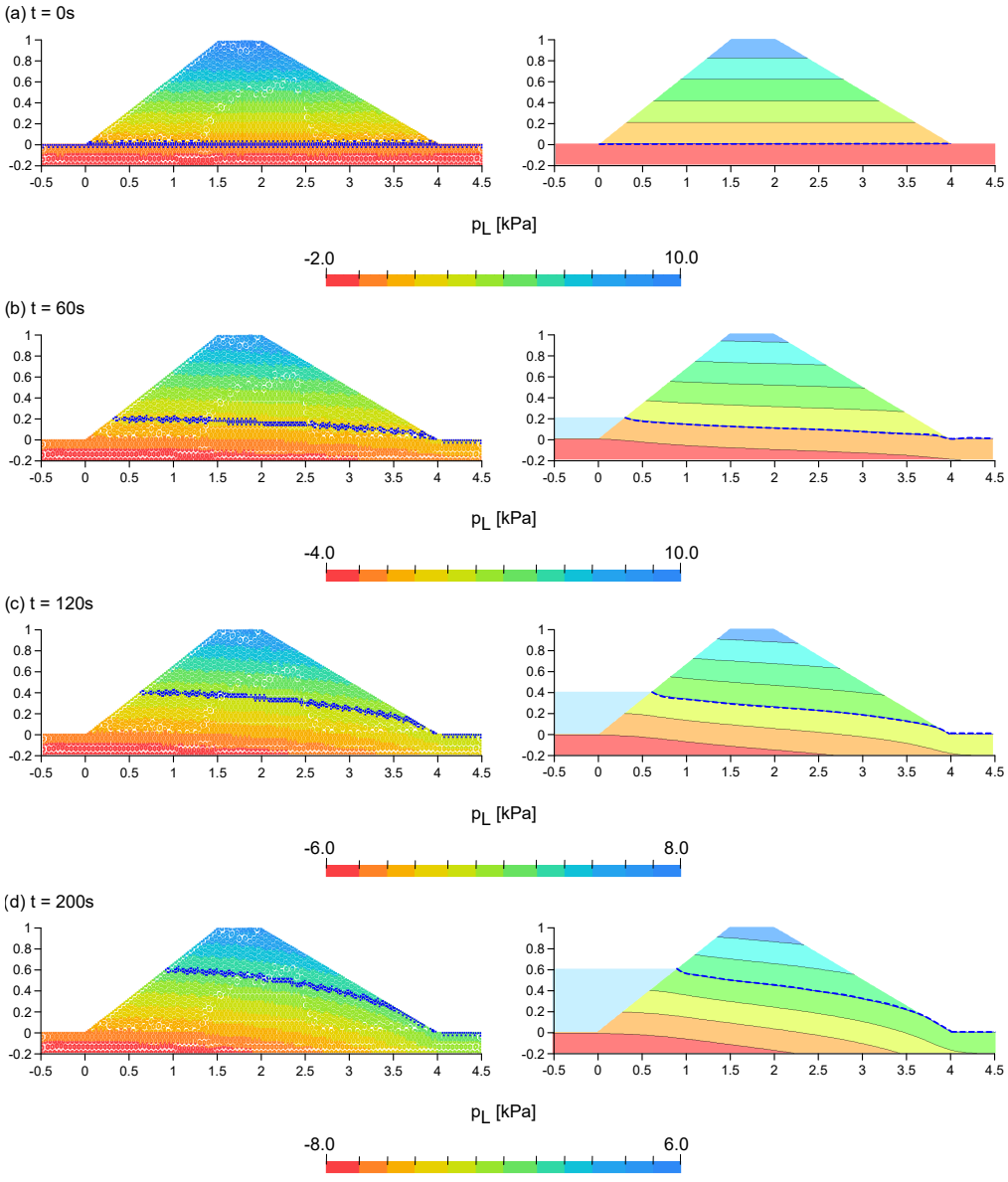

Figure 6: Evolution of liquid pressure in the levee body. Comparison between MPM (left) and FEM (right).

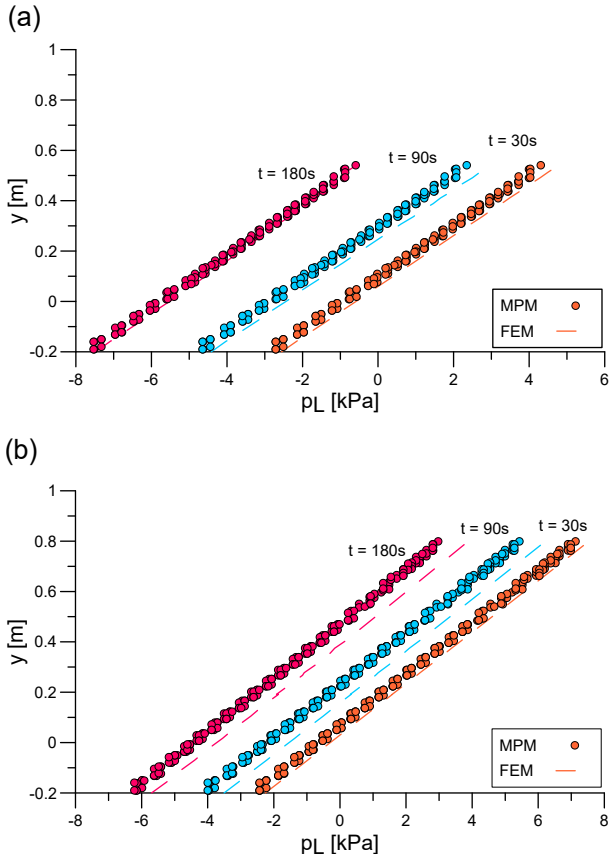

Figure 7: Pore pressure along vertical sections S1 (a) and S2 (b) for MPM (dots) and FEM (dashed line).

parameters listed in Tab. 2. Cohesion and friction angle in unsaturated soils are function of suction, but this effect is assumed negligible in this example. Although the constitutive model is simple, it can provide a realistic representation of the levee response; more advanced constitutive models will be used in further development of this research.

5.1. Levee failure for rapid drawdown

The initial stress distribution is generated with gravity loading assuming a river level at 2.0m. Then, the applied total head is rapidly decreased to the low water level of 0.5m (Fig. 9).

As introduced in Sec. 3.3.1, the present study imposes the pore pressure at the boundary above the river level in two different manners, constant or linear. Two simulations starting from an identical state, are used to compare the effects of both approximations when the slope is subjected to a drawdown (Fig. 10). The linear approximation generates high suction values in the top portion of the river bank, preventing the slope instability (bottom panels in Fig. 10). In the constant approximation, a pressure of 5kPa is applied at the points above water level. This lower value of suction leads to the failure of the embankment during drawdown (top panels in Fig. 10). Note that, if measurements of suction data collected on river levee along time are

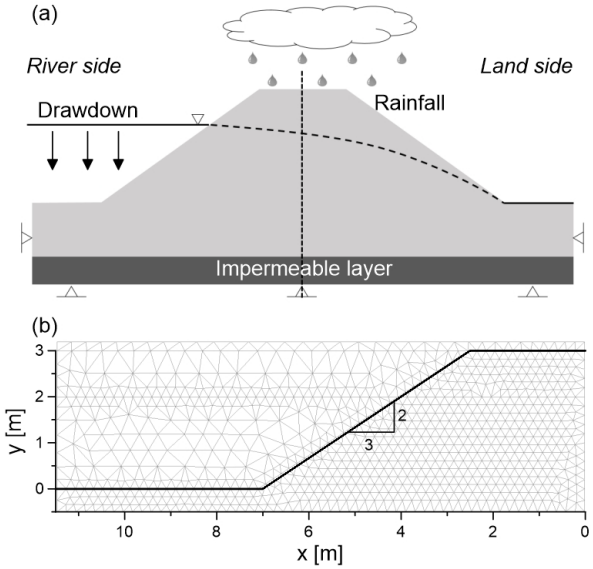

Figure 8: (a) Simplified representation of the levee example. (b) Geometry and discretization of the MPM model.

Solid density $[kg/m^3]$	ρ_S	2700
Liquid density $[kg/m^3]$	ρ_L	1000
Porosity [-]	n	0.4
Liquid bulk modulus $[kPa]$	K_L	80000
Liquid dynamic viscosity $[1/kPa]$	μ_L	$1 \cdot 10^{-6}$
Intrinsic permeability $[m^2/s]$	κ_L	$4 \cdot 10^{-11} m^2/s$
Young modulus $[kPa]$	E	50000
Poisson ratio [-]	ν	0.30
Friction angle [°]	ϕ	27
Cohesion $[kPa]$	c'	2

Table 2: Material parameters for levee collapse example.

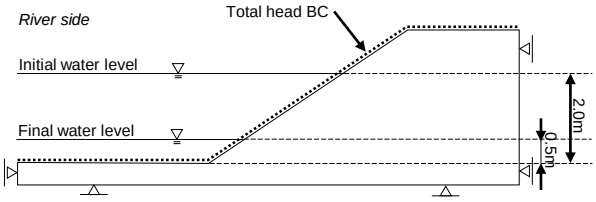

Figure 9: Geometry and boundary condition of the model simulating drawdown on a levee.

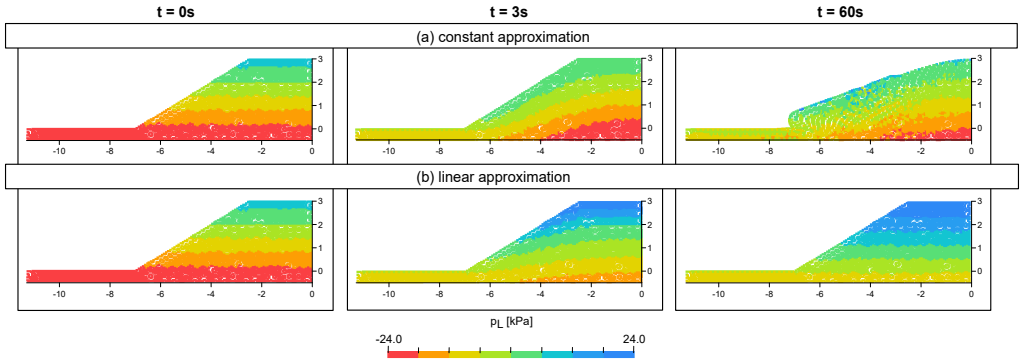

Figure 10: Evolution of liquid pore pressure at 0, 3, and 60s considering different pore pressure distributions (hydraulic head BC) above the current river level, related to (a) constant, (b) linear approximations.

available for a real case study, it is possible to set the constant approximated value based on the real initial condition. The constant approximation is compared with the FEM-LEM results.

In order to emphasise the hydromechanical character of the depicted process, the onset of failure and the concurrent pore pressure distribution for MPM and FEM-LEM analyses are presented in Fig.11. For MPM, the norm of solid displacement is used to show the development of the slip surface, while in the LEM the circular surface is automatically generated, just by imposing ranges of entry and exit, and the relative FS is obtained. The failure onset is identified in LEM by the FS passage to a value lower than one, while in MPM it is here identified when the deviatoric strain assumes a value equal to 0.05 and at the same time vertical displacements of the cm-order can be detected at the MPs on the levee crest. The shape of the slip surface is consistent among the two models. The occurrence time of the failure onset differs for a few seconds, which can be explained by looking at the pore pressure distribution above the current river level, as visible in Fig. 11. This difference can be explained because in the MPM simulation, a constant pressure is imposed along the boundary portion above the river height, while in FEM a potential seepage BC is applied instead [37].

Only for MPM it is possible to track the river bank collapse progression along time, likewise the pore pressure dissipation process. The post-failure behavior is captured in Fig. 12 by plotting the horizontal solid displacements at three time instants, together with the initial soil surface elevation reference. The phenomenon is clearly characterized by large displacements, at the end exceeding 1m (Fig. 12c); thus the irreversible collapse of the internal bank is determined. Three MPs nearby the slip surface (MP1, MP2, MP3) are tracked during the slope motion in Fig. 12 and used to analyze the evolution of liquid pressure (Fig. 13a) and deviatoric strain (Fig. 13b) along time.

In the first 3 seconds, all the MPs experience a sudden reduction of liquid pressure as a result of the dynamics induced by the rapid drawdown. It is followed by a gentle pressure increase till 20s, and a subsequent interval of pressure oscillations. In general, the pore pressure values reflect the overall state of slow desaturation of the slope, antithetic to the rapid kinematic process of slope instability. Concerning this last, the deviatoric strain curves which represent the progressive increase of MPs undergoing plastification around the slip surface area, follow a continuous increase till maximum values is reached at 60s. In addition, the graph shows that from the slope crest towards the toe, the MPs deformation magnitude coherently increases.

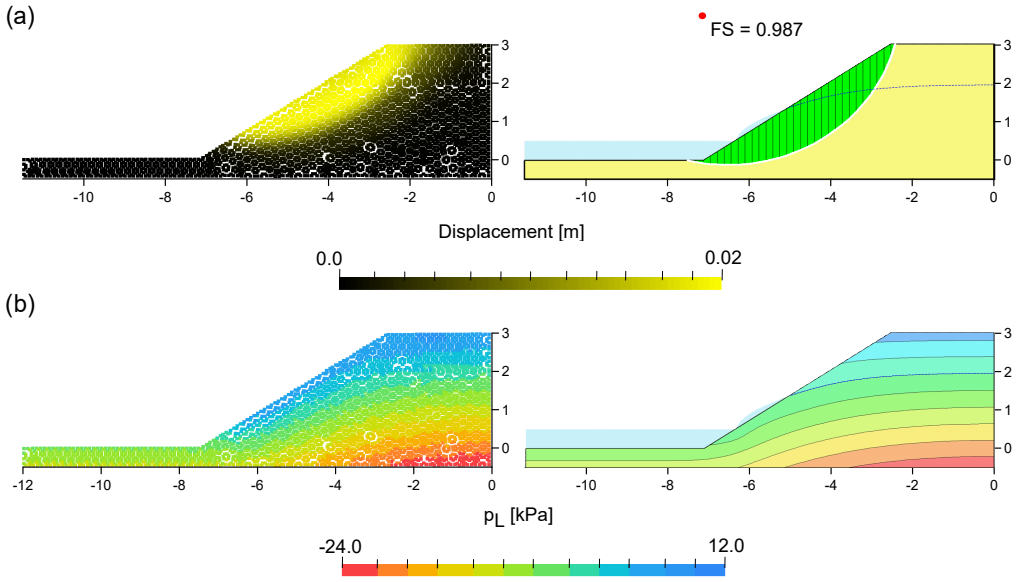

Figure 11: Onset of failure: a) Solid displacement norm for MPM and critical slip surface for FEM-LEM b) Concurrent liquid pressure in the same moment.

5.2. Levee failure for rainfall infiltration

Enduring high water level on the river side and heavy rainfall can sometimes concur leading to rapid saturation of the levee and potential instability. The geometry and boundary condition of the numerical model are shown in Fig. 14. At the right-end, a liquid pressure linearly increasing with depth (hydrostatic pressure distribution) is applied to reproduce in a simplified way a water level of 2.0m on the river side. The levee surface is a potential seepage face during the initialization phase, and then an infiltration rate $\widehat{w_y} = 1 \cdot 10^{-4} m/s$ is applied to simulate a heavy rainfall in the following steps. Horizontal fixities are applied to the solid phase at the lateral boundaries and the bottom is fully fixed.

To generate the initial stress distribution, liquid pressure, seepage face and gravity load are applied assuming an initially high material cohesion (20kPa). Then, cohesion is reduced to 2kPa and the slope is stable with a stress distribution in equilibrium with the applied initial loads. The initial pore pressure distribution obtained with MPM and FEM is in very good agreement (Fig. 15). FS evaluated with Bishop method is higher than 1, and indeed the slope is stable and deformations are very small.

After stress initialization, rainfall infiltration is applied at the top surface, soil suction decreases and the slope fails. LEM analyses give $FS < 1$ for a time $t = 15s$, which means that the failure surface is fully developed at this moment. Fig. 16 plots the evolution of shear strain at significant time instants, showing that a circular failure surface develops rapidly from the bottom of the slope and propagates upward. The shape of the failure surface is in agreement with LEM; however, in MPM it is a result of the calculation, while in LEM it is an hypothesis of the analysis.

A small decrease of suction is sufficient to trigger the failure as shown in Fig. 17. During soil movement, pressure oscillations are observed. Displacements increase suddenly between 5 and 20s (Fig. 18). At t=20s the slope finds a new equilibrium configuration measuring 17cm

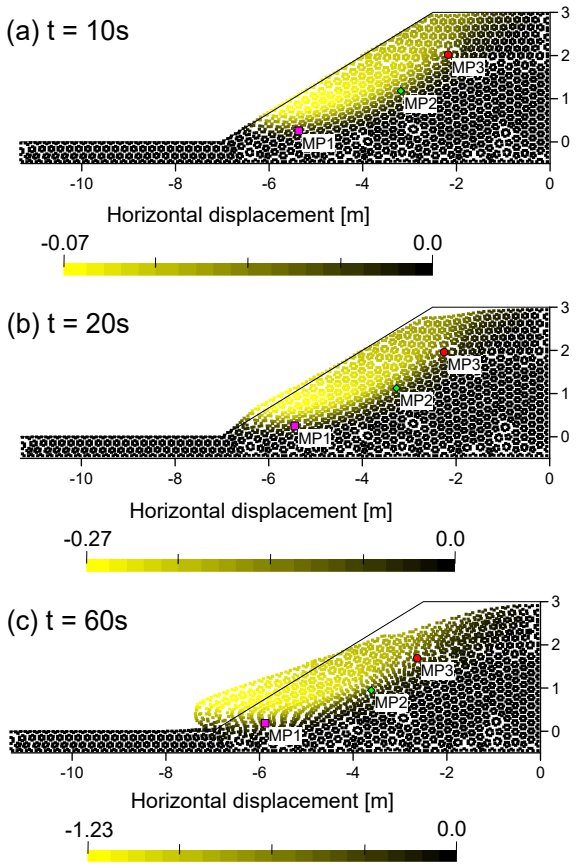

Figure 12: Horizontal displacement contours at 10s, 20s and 60s. Identification of MP1, MP2, MP3 along the slip surface.

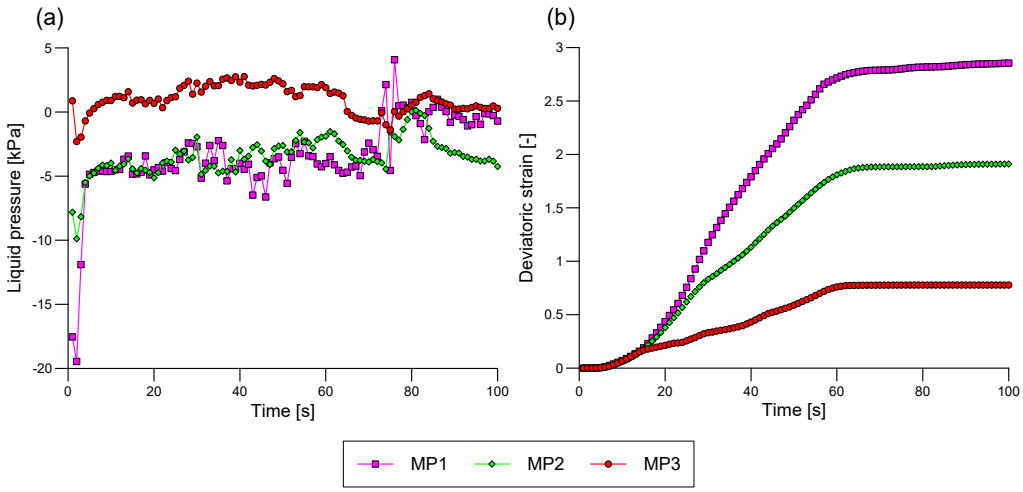

Figure 13: Liquid pore pressure (a) and deviatoric strain (b) along time for three selected MPs nearby the slip surface.

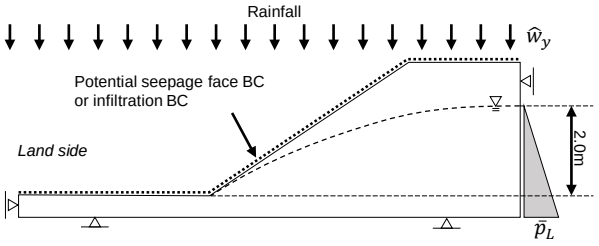

Figure 14: Geometry and boundary condition of the model simulating rainfall infiltration on a levee.

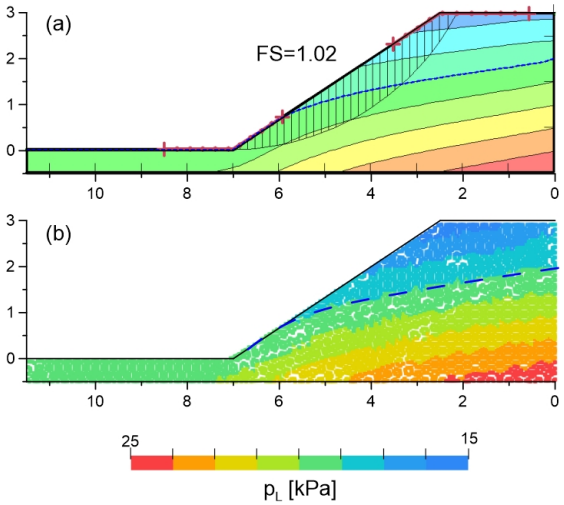

Figure 15: Initial pore pressure distribution with (a) FEM and (b) MPM. Safety factor with LEM.

of displacement of the toe and 25cm at the crest. At about 100s there is a further increase of displacement of 2cm due to enduring rainfall infiltration. The crest of the levee moves downward approximately 22cm, which means that the levee in its deformed configuration is probably still able to fulfill its retaining function. This consideration, impossible to get with FEM or LEM, can have significant practical consequences for planning of cost-effective remedial measures.

6. Conclusions

This paper presents a two-phase single point formulation of MPM for unsaturated materials and discusses in detail the application of hydraulic boundary conditions for the simulation of common geotechnical problems such as transient total head, infiltration/evaporation, and potential seepage face. The method is validated with a 1D infiltration test and a 2D seepage problem and applied to study a levee collapse due to rapid drawdown and heavy rainfall.

This method allows to investigate the consequences of slope instabilities, thanks to the possibility of simulating large deformations, thus overtaking the concept of safety factor customarily estimated by LEMs or FEMs. In contrast to these methods, MPM allows to get a realistic estimate of soil movements. The levee example shows that, depending on the boundary conditions, similar values of FS, slightly lower than one, can lead to different displacement evolution after failure initiation and thus different consequences in terms of risk assessment. Different scenarios could be investigated modifying the geometry and mechanical behavior of the soil. Taking into account these aspects is important to implement safe and cost effective mitigation measures.

7. Acknowledgments

Financial support from Fondazione Ing. Aldo Gini and University of Padua (BIRD181859) is gratefully acknowledged.

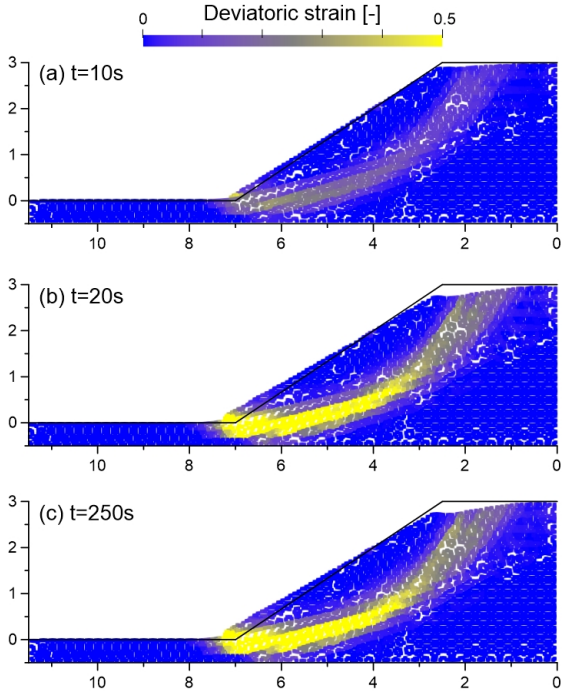

Figure 16: Deviatoric strain contour at different time instant.

8. CRediT roles

F. Ceccato: Conceptualization, Methodology, Software, Validation, Writing - Original Draft, Writing - Review & Editing. A. Yerro: Conceptualization, Methodology, Software, Validation, Writing - Original Draft, Writing - Review & Editing. V. Girardi: Conceptualization, Methodology, Software, Validation, Writing - Original Draft, Writing - Review & Editing. P. Simonini: Supervision, Writing - Review & Editing, Funding acquisition

References

[1] D. V. Griffiths, P. A. Lane, Slope stability analysis by finite elements, Geotechnique 49 (1999) 387–403. doi:10.1680/geot.1999.49.3.387.

[2] J. Duncan, State of the art: limit equilibrium and finite-element analysis of slopes, Journal of Geotechnical engineering (1996) 577–596.

[3] K. Soga, E. Alonso, A. Yerro, K. Kumar, S. Bandara, Trends in large-deformation analysis of landslide mass movements with particular emphasis on the material point method, Géotechnique 66 (2016) 248–273. URL: http://dx.doi.org/10.1680/jgeot.15.LM.005] http://www.icevirtuallibrary.com/doi/10.1680/jgeot.15.LM.005. doi:10.1680/jgeot.15.LM.005.

[4] A. Yerro, E. E. Alonso, N. M. Pinyol, The material point method for unsaturated soils, Geotechnique 65 (2015) 201–217. URL: http://www.icevirtuallibrary.com/doi/10.1680/geot.14.P.163. doi:10.1680/geot.14.P.163.

[5] S. Bandara, K. Soga, Coupling of soil deformation and pore fluid flow using material point method, Computers and Geotechnics 63 (2015) 199–214. URL: http://linkinghub.elsevier.com/retrieve/pii/S0266352X14001839. doi:10.1016/j.compgeo.2014.09.009.

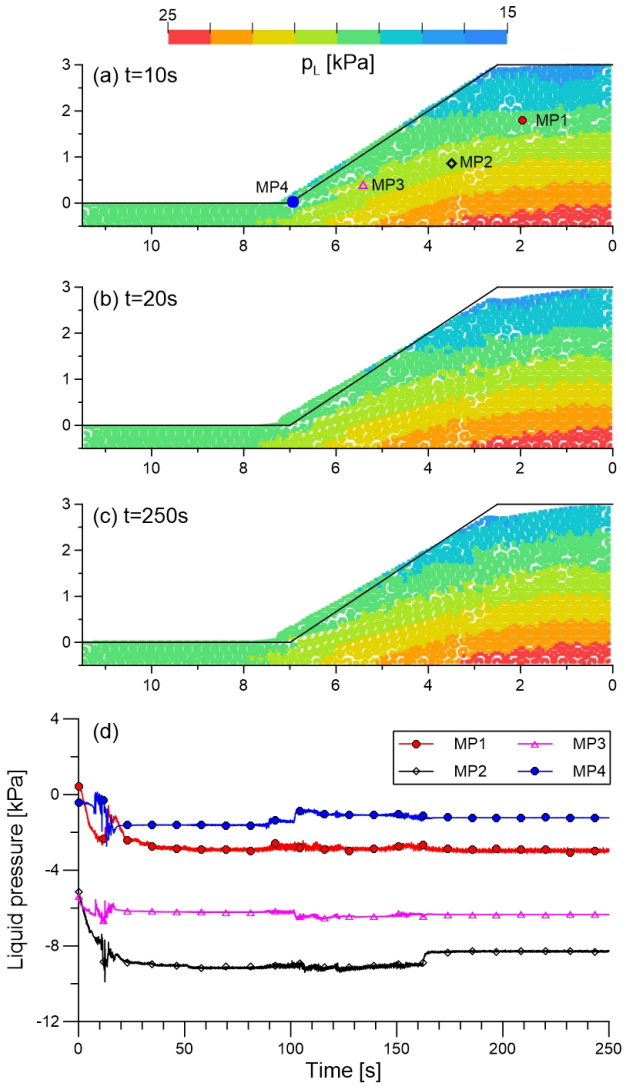

Figure 17: (a-c) Pore pressure contour at different time instant. (d) Pore pressure along time for four MP.

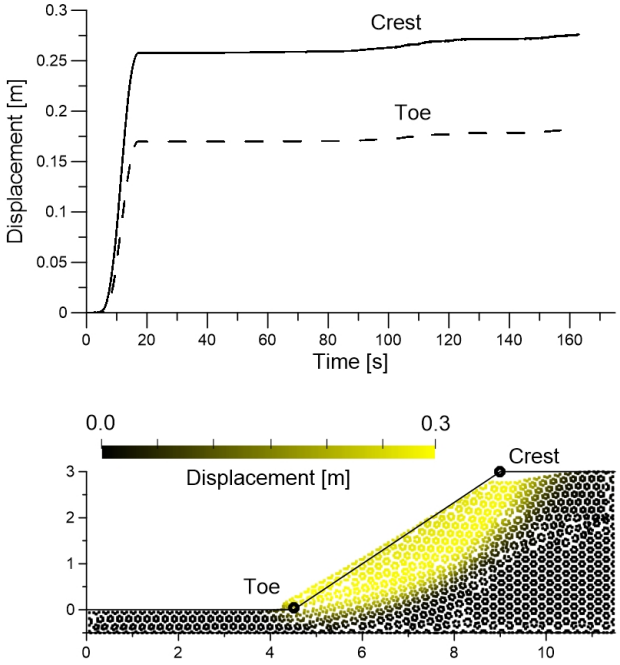

Figure 18: Evolution of displacement with time and final displacement contour.

[6] F. Ceccato, P. Simonini, Numerical study of partially drained penetration and pore pressure dissipation in piezocone test, Acta Geotechnica 12 (2016) 195–209. URL: http://dx.doi.org/10.1007/s11440-016-0448-6. doi:10.1007/s11440-016-0448-6.

[7] S. Bandara, A. Ferrari, L. Laloui, Modelling landslides in unsaturated slopes subjected to rainfall infiltration using material point method, International Journal for Numerical and Analytical Methods in Geomechanics 40 (2016) 1358–1380.

[8] F. Ceccato, V. Girardi, P. Simonini, Developing and testing multiphase mpm approaches for the stability of dams and river embankments, in: Conference of the Italian Association of Theoretical and Applied Mechanics, Springer, 2019, pp. 2179–2195.

[9] N. M. Pinyol, M. Alvarado, E. E. Alonso, F. Zabala, Thermal effects in landslide mobility, Géotechnique 68 (2017) 1–18. URL: https://doi.org/10.1680/jgeot.17.P.054 http://www.icevirtuallibrary.com/doi/10.1680/jgeot.17.P.054. doi:10.1680/jgeot.17.P.054.

[10] B. Wang, P. J. Vardon, M. A. Hicks, Rainfall-induced slope collapse with coupled material point method, Engineering Geology 239 (2018) 1–12. URL: https://doi.org/10.1016/j.enggeo.2018.02.007. doi:10.1016/j.enggeo.2018.02.007.

[11] X. Lei, S. He, X. Chen, H. Wong, L. Wu, E. Liu, A generalized interpolation material point method for modelling coupled seepage-erosion-deformation process within unsaturated soils, Advances in Water Resources 141 (2020) 103578. doi:10.1016/j.advwatres.2020.103578.

[12] D. Sulsky, Z. Chen, H. Schreyer, A particle method for hystory-dependent materials, Computer Methods in Applied Mechanics and Engineering 118 (1994) 179–196.

[13] O. C. Zienkiewicz, A. H. C. Chan, M. Pastor, B. A. Schrefler, T. Shiomi, Computational geomechanics, Wiley Chichester, 1999.

[14] F. Ceccato, V. Girardi, A. Yerro, P. Simonini, Evaluation of dynamic explicit MPM formulations for unsaturated soils, in: E. Oñate, M. Bischoff, D. Owen, P. Wriggers, T. Zohdi (Eds.), Particles 2019, Barcellona, 2019.

[15] J. van Esch, D. Stolle, P. Bonnier, O. C. Lsl, Consideration of Pore Pressures in MPM, in: Computer Methods in Mechanics, May, 2009, pp. 1–16.

[16] A. Chmelnizkij, F. Ceccato, J. Grabe, P. Simonini, 1D wave propagation in saturated soils : verification of two-phase MPM, in: 2nt international conference on the Material Point Method for modelling soil-water-structure

interaction, 2019.
[17] I. Jassim, D. Stolle, P. Vermeer, Two-phase dynamic analysis by material point method, International Journal for Numerical and Analytical Methods in Geomechanicsnumerical and analytical methods in Geomechanics 37 (2013) 2502–2522. URL: http://onlinelibrary.wiley.com/doi/10.1002/nag.2146/full. doi:10.1002/nag.
[18] A. Yerro, E. Alonso, N. Pinyol, Modelling large deformation problems in unsaturated soils, in: E-UNSAT 2016, volume 9, 2016, pp. 1–6. doi:10.1051/e3sconf/20160908019.
[19] A. Gens, M. Sánchez, D. Sheng, On constitutive modelling of unsaturated soils, Acta Geotechnica 1 (2006) 137–147. doi:10.1007/s11440-006-0013-9.
[20] S. K. Vanapalli, D. G. Fredlund, D. E. Pufahl, A. W. Clifton, Model for the prediction of shear strength with respect to soil suction, Canadian Geotechnical Journal 33 (1996) 379–392. doi:10.1139/t96-060.
[21] B. Loret, N. Khalili, A three-phase model for unsaturated soils, International Journal for Numerical and Analytical Methods in Geomechanics 24 (2000) 893–927. doi:10.1002/1096-9853(200009)24:11¡893::AID-NAG105¿3.0.CO;2-V.
[22] D. Mašín, N. Khalili, A hypoplastic model for mechanical response of unsaturated soils, International Journal for Numerical and Analytical Methods in Geomechanics 32 (2008) 1903–1926. doi:10.1002/nag.714.
[23] D. Sheng, S. W. Sloan, A. Gens, A constitutive model for unsaturated soils: Thermomechanical and computational aspects, Computational Mechanics 33 (2004) 453–465. doi:10.1007/s00466-003-0545-x.
[24] B. Francois, L. Laloui, Acmeg-ts: A constitutive model for unsaturated soils under non-isothermal conditions, International Journal for Numerical and Analytical Methods in Geomechanics 32 (2008) 1955–1988. doi:10.1002/nag.712.
[25] D. Hillel, Soil and water – physical principles and processes, Academic press, London (UK), 1971.
[26] Y. Mualem, Hysteretical models for prediction of the hydraulic conductivity of unsaturated porous media, Water Resources Research 12 (1976) 1248–1254. URL: http://doi.wiley.com/10.1029/WR012i006p01248. doi:10.1029/WR012i006p01248.
[27] M. M. J. Mieremet, D. F. Stolle, F. Ceccato, C. Vuik, Numerical stability for modelling of dynamic two-phase interaction, International Journal for Numerical and Analytical Methods in Geomechanics 40 (2015). doi:DOI: 10.1002/nag.2483.
[28] M. M. J. Mieremet, Numerical stability for velocity-based 2-phase formulation for geotechnical dynamic analysis, Report 15-03, {ISSN} 1389-6520, Reports of the Delft Institute of Applied Mathematics, Delft University of Technology, Delft, The Netherlands, 2015.
[29] D. Sulsky, S.-J. Zhou, H. L. Schreyer, Application of a particle-in-cell method to solid mechanics, Computer Physics Communications 87 (1995) 236–252. URL: http://linkinghub.elsevier.com/retrieve/pii/0010465594001707. doi:10.1016/0010-4655(94)00170-7.
[30] C. Scudeler, C. Paniconi, D. Pasetto, M. Putti, Examination of the seepage face boundary condition in subsurface and coupled surface/subsurface hydrological models, Water Resources Research 53 (2017) 1799–1819. doi:10.1111/j.1752-1688.1969.tb04897.x.
[31] R. Hu, Y. Chen, C. Zhou, H.-H. Liu, A numerical formulation with unified unilateral boundary condition for unsaturated flow problems in porous media, Acta Geotechnica (2016). doi:10.1007/s11440-016-0475-3.
[32] Y.-M. Hong, S. Wan, Forecasting groundwater level fluctuations for rainfall-induced landslide, Natural Hazards 57 (2011) 167–184.
[33] A. Hendron Jr, F. D. Patton, The vaiont slide. A geotechnical analysis based on new geologic observations of the failure surface. Volume 1. Main text, Technical Report, ARMY ENGINEER WATERWAYS EXPERIMENT STATION VICKSBURG MS GEOTECHNICAL LAB, 1985.
[34] N. Lu, W. Likos, K. (Firm), Unsaturated Soil Mechanics, Wiley, 2004. URL: https://books.google.com/books?id=Rv1RAAAAMAAJ.
[35] D. V. Griffiths, N. Lu, Unsaturated slope stability analysis with steady infiltration or evaporation using elasto-plastic finite elements, International Journal for Numerical and Analytical Methods in Geomechanics 29 (2005) 249–267. doi:10.1002/nag.413.
[36] H. Rahardjo, A. Satyanaga, E. C. Leong, Effects of flux boundary conditions on pore-water pressure distribution in slope, Engineering Geology 165 (2013) 133–142. URL: http://dx.doi.org/10.1016/j.enggeo.2012.03.017. doi:10.1016/j.enggeo.2012.03.017.
[37] Geoslope, Stability Modeling with SLOPE / W 2007 Version, 2010.
[38] C. Callari, A. D. Abati, Finite element methods for unsaturated porous solids and their application to dam engineering problems (2009).
[39] P. Simonini, S. Cola, S. Bersan, Caratterizzazione geotecnica, meccanismi di collasso e monitoraggio degli argini fluviali - relazione generale, 2014.
[40] Y. Deniaud, H. van Hemert, J. McVicker, A. Bernard, B. Beullac, R. Tourment, M. Igigabel, R. Pohl, M. Sharp, J. Simm, et al., Functions, forms and failure of levees, CIRIA, 2013.

[41] P. Peter, Canal and River Levées, ISSN, Elsevier Science, 2014. URL: https://books.google.com/books?id=aQ9BAQAAQBAJ.